



Published in final edited form as:

*J Mol Biol.* 2016 January 16; 428(1): 10–25. doi:10.1016/j.jmb.2015.09.031.

## The structural basis of actin organization by vinculin and metavinculin

Laura Y. Kim<sup>a</sup>, Peter M. Thompson<sup>b</sup>, Hyunna T. Lee<sup>b</sup>, Mihir Pershad<sup>c</sup>, Sharon L. Campbell<sup>b</sup>, and Gregory M. Alushin<sup>b,d</sup>

<sup>a</sup>Laboratory of Macromolecular Interactions, Cell Biology and Physiology Center, National Heart Lung and Blood Institute, National Institutes of Health, Bethesda, MD, 20892, USA

<sup>b</sup>Department of Biochemistry and Biophysics, University of North Carolina at Chapel Hill, Chapel Hill, NC 27599, USA

<sup>c</sup>Department of Chemistry, University of North Carolina at Chapel Hill, Chapel Hill, NC, 27599, USA

### Abstract

Vinculin is an essential adhesion protein that links membrane-bound integrin and cadherin receptors through their intracellular binding partners to filamentous actin, facilitating mechanotransduction. Here we present an 8.5 Å resolution cryo-EM reconstruction and pseudo-atomic model of the vinculin tail (Vt) domain bound to F-actin. Upon actin engagement, the N-terminal “strap” and helix 1 are displaced from the Vt helical bundle to mediate actin bundling. We find that an analogous conformational change also occurs in the H1' helix of the tail domain of metavinculin (MVt) upon actin binding, a muscle-specific splice isoform which suppresses actin bundling by Vt. These data support a model in which metavinculin tunes the actin bundling activity of vinculin in a tissue-specific manner and provide a mechanistic framework for understanding metavinculin mutations associated with hereditary cardiomyopathies.

### Graphical abstract

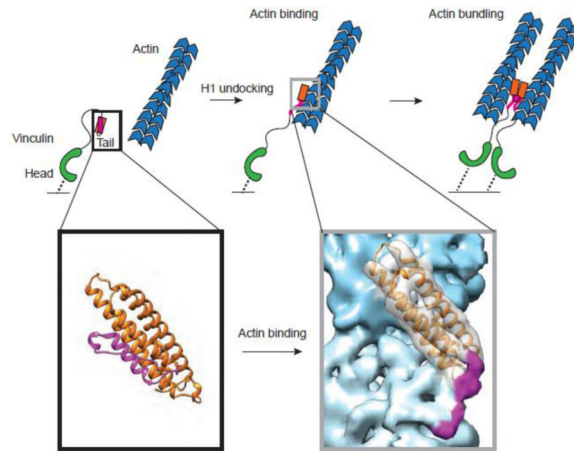
---

<sup>d</sup>Correspondence should be addressed to G.M.A. (alushing@mail.nih.gov).

**Publisher's Disclaimer:** This is a PDF file of an unedited manuscript that has been accepted for publication. As a service to our customers we are providing this early version of the manuscript. The manuscript will undergo copyediting, typesetting, and review of the resulting proof before it is published in its final citable form. Please note that during the production process errors may be discovered which could affect the content, and all legal disclaimers that apply to the journal pertain.

#### Accession Codes

Cryo-EM density maps have been deposited in the Electron Microscopy Databank with the following accession codes: Vt C5-bound actin, EMD-6446; MVt C5-bound actin, EMD-6447; actin alone, EMD-6448; Vt C5-GFP bound actin, EMD-6450; GFP-E892-Vt C5 bound actin, EMD-6451; unsharpened Vt C5-bound actin (for calculating difference maps), EMD-6449. Corresponding MDFF models have been deposited in the Protein Databank with the following accession codes: Vt-actin, 3JBI, MVt-actin, 3JBK, actin alone, 3JBJ.



## Keywords

Cryo-EM; Cytoskeleton; Mechanobiology; Adhesion; Cell motility

## Introduction

Vinculin is a highly conserved and essential adhesion scaffolding protein that physically links membrane-bound integrin and cadherin receptors through their intracellular binding partners to filamentous actin<sup>1; 2; 3</sup>. It plays a critical role in mechanotransduction, as vinculin is recruited to and stabilizes adhesions in response to force, regulates the dynamics of adhesions at the leading edge of migrating mesenchymal cells, and mediates the transmission of traction forces<sup>4; 5; 6; 7; 8; 9; 10</sup>. These functions are essential for viability, as genetic ablation in the mouse results in embryonic lethality at E10, with severe defects in heart development and neural tube closure<sup>11</sup>. Fibroblasts isolated from knockout mice demonstrate enhanced cytoskeletal dynamics<sup>6</sup> and increased migration velocities in culture<sup>6; 11</sup>, suggesting a critical role for vinculin in regulated cell migration during development.

Vinculin is a 117 kDa alpha-helical protein with no known catalytic activity. It is composed of a large 91 kDa N-terminal “head” domain (Vh) and small 21 kDa C-terminal “tail” domain (Vt) connected by a 4.6 kDa, flexible proline-rich linker<sup>12; 13; 14</sup>. Mechanistically, vinculin facilitates mechanotransduction through interactions with at least 19 binding partners to coordinate intracellular signaling<sup>2</sup> and strengthen the physical connection between membrane receptors and the actin cytoskeleton<sup>1; 2; 3</sup>. This mechanical reinforcement is primarily mediated by vinculin’s interactions with talin<sup>15</sup>, a critical integrin binding protein, which binds the Vh domain<sup>16</sup>, and F-actin<sup>17</sup>, which binds the Vt domain<sup>18</sup>. In isolation<sup>12</sup> and in the bulk cytoplasm<sup>19</sup> full-length vinculin adopts an auto-inhibited conformation, with a nanomolar-affinity interaction formed between the head and tail domains<sup>20</sup>, masking the Vt actin binding site<sup>20; 21</sup>. Auto-inhibition is relieved by vinculin engaging in simultaneous protein-protein interactions with multiple binding partners<sup>22</sup>. A structure of a subdomain of Vh bound to a fragment of talin displayed a conformation sterically incompatible with the head-tail interaction<sup>23</sup>, supporting an allosteric mechanism

of activation. Each talin molecule contains multiple cryptic vinculin binding sites, which can be revealed upon the application of tension across the talin molecule<sup>24</sup>. A model has thus been proposed wherein increasing traction force in an adhesion results in the accumulation of vinculin and reinforcement of the adhesion-cytoskeleton linkage, supported by the recent finding that vinculin accumulates in substantial stoichiometric excess to other components as an adhesion grows<sup>25</sup>.

In addition to binding actin, the isolated Vt domain bundles filaments, inducing the formation of dense actin fibers<sup>17; 26</sup>. Both activities are required for vinculin function *in vivo*, as lesions that selectively disrupt them in the context of the full-length molecule lead to defects in cell spreading, adhesion formation and maturation, and mechanotransduction<sup>6; 27; 28; 29</sup>. Cross-linking and tomographic studies indicate that actin bundling occurs through oligomerization of the Vt domain<sup>26; 27; 30</sup>. Vt primarily exists as a soluble monomer *in vitro* at physiological concentrations<sup>31</sup>, suggesting that actin binding results in a conformational change to reveal a cryptic dimerization interface by an unknown mechanism<sup>30</sup>. Previous negative stain reconstructions of Vt bound to F-actin have given rise to contradictory propositions for the interaction interface<sup>26; 28</sup>, due to challenges in unambiguously docking the pseudo-symmetric barrel-shaped Vt structure into low-resolution envelopes. Therefore, the functionally critical and interrelated mechanisms of Vt actin binding and actin bundling remain unresolved, despite substantial scrutiny.

Metavinculin, a larger splice isoform which is co-expressed with vinculin in cardiac and smooth muscle, has been implicated in cardiomyopathies<sup>32; 33; 34</sup> and atherosclerosis<sup>35</sup>. Disease mutations are found in the 68 amino-acid splice insertion<sup>32; 34</sup>, which occurs after vinculin amino acid 915, between helices 1 and 2 of Vt. Structural studies have shown that a portion of the insertion replaces the first (H1) of the five helices composing the Vt helical bundle, adopting a nearly identical helical conformation (H1') despite its distinct sequence<sup>36</sup>. The sequence comprising H1 was not visible in the crystallographic electron density maps, presumably becoming an unstructured element along with the rest of the linker connecting the head and tail domains. Although investigations of metavinculin have been limited, previous studies suggest that the metavinculin tail domain (MVt) possesses similar actin binding to Vt but diminished actin bundling activity<sup>32; 37; 38</sup>, as well as the intriguing property of suppressing actin bundling by Vt<sup>38</sup>. Disease mutations in MVt produce higher-order actin assemblies with aberrant architectures *in vitro*<sup>32</sup>, suggesting that a detailed mechanistic understanding of Vt- and MVt-actin interactions will provide insight into the molecular basis of these pathologies.

Here we present sub-nanometer-resolution reconstructions of Vt and MVt bound to actin, sufficient for the generation of pseudo-atomic models of both interfaces. We find that Vt H1 is displaced from the helical bundle upon actin binding, and mutagenesis of a buried residue in H1 in the pre-bound state suggests that this region must become solvent-accessible to mediate actin bundling. The remainder of the bundle undergoes a torqueing conformational change to relieve clashes with its binding site on actin. In contrast, actin does not undergo any significant rearrangements. MVt undergoes a similar structural transition, displacing helix H1' to form an interaction with actin that is indistinguishable from Vt at the resolution of our reconstructions. Additionally, we find that the presence of sub-stoichiometric MVt

suppresses the actin-bundling activity of Vt, in support of a recent study<sup>38</sup>. We interpret these results in a conceptual model wherein vinculin and metavinculin undergo partial unfolding transitions commensurate with actin engagement, which can either lead to the promotion or suppression of actin bundling depending on the presence of the MVt insertion.

## Results

### Cryo-EM reconstruction of the Vt-F-actin complex

To visualize the vinculin-actin interface, we pursued cryo-EM studies of the Vt-actin complex (Fig. 1). To prevent Vt-mediated bundling<sup>27</sup>, which is refractory to structural studies, we employed a C-terminal truncation mutant (residues 879–1061 of chicken vinculin, hereafter referred to as Vt C5). Vt has relatively low affinity for F-actin ( $\sim 0.5 \mu\text{M}^{21}$ ), making it technically challenging to fully decorate filaments. Furthermore, Vt-bound filaments are essentially indistinguishable by eye from unbound filaments in low-contrast images, resulting in a mixed population of decorated and undecorated filaments that cannot easily be sorted by selective picking of filaments for processing, or by reference-free 2D classification of filament segments (Fig. 1a, b). A reconstruction calculated from the entire dataset produced a volume that clearly showed sub-stoichiometric occupancy for Vt C5 (Fig. 1c).

We therefore adapted a multi-reference Iterative Helical Real Space Reconstruction (IHRSR)<sup>39</sup> scheme we recently developed for the study of heterogeneous microtubule specimens<sup>40</sup> (Fig. 1c). We collected and processed a dataset of undecorated F-actin filaments, then subjected our Vt C5-bound dataset to a multi-reference IHRSR in EMAN2 / SPARX<sup>41; 42</sup> using the sub-stoichiometrically bound and unbound models as references. This resulted in a Vt C5-bound model with substantially improved occupancy. Segments which contributed to this model were selected for further processing using FREALIGN<sup>43</sup>, which produced an 8.5 Å resolution reconstruction (gold-standard FSC 0.143, Supplementary Fig. 1d) with clearly resolved secondary structure for both actin and Vt C5 (Fig 2a).

### Vt undergoes a structural rearrangement upon actin engagement

Vt in isolation<sup>44</sup> and in the context of full-length vinculin<sup>12</sup>, adopts a 5-helix bundle fold with C-terminal and N-terminal extensions, including a small C-terminal hairpin and N-terminal coil “strap”. Unexpectedly, we observed only 4 helical densities that were not attributable to actin (Fig. 2a, orange), suggesting that one helix is displaced from the bundle upon actin engagement. Rigid-body docking of the isolated Vt crystal structure (PDB 1QKR<sup>44</sup>, Fig. 2b) quantitatively supported the interaction pose produced using discrete molecular dynamics in the recent study of Thompson et al.<sup>28</sup>, in which helices 4 and 5 constitute the primary binding interface, engaging two longitudinally adjacent actin protomers (Supplementary Fig. 1, Supplementary Movie 1, 2). This model suggests that helix 1 disengages from the helical bundle upon actin binding, supported by recent biochemical evidence that this segment becomes susceptible to proteolytic cleavage upon actin binding by Vt<sup>38</sup>.

We also observed a small amount of additional density on the filament surface that was not explained by the docked crystal structures of Vt or actin (Fig. 2b, magenta), suggesting that the H1 region and / or the flexible C-terminal hairpin could form an additional contact with actin. To test this hypothesis, we performed mass-tagging experiments to localize these regions of the protein (Supplementary Fig. 2). We generated cryo-EM reconstructions of Vt C5 constructs bound to F-actin with GFP fused at the C-terminus (Vt C5-GFP, 19.2 Å gold-standard FSC 0.143), and N-terminal to helix 1 (GFP-E892-Vt C5, 16.4 Å gold-standard FSC 0.143). Amplitude-weighted difference maps calculated versus the wild-type Vt C5 reconstruction showed positive density adjacent to subdomain 2 of actin 1 in both cases (Fig. 2b), suggesting that both regions of the protein contribute to the density and engage the actin surface. This conformation of the C-terminus is consistent with the recent report that R1049 is important for actin binding<sup>29</sup>, bringing this residue close to the negatively charged surface of subdomain 2 (Fig. 2c).

In addition to the displacement of helix 1, the rigid-body fit of helices 2–5 showed inconsistencies with the density map, including a clash between the N-terminal tip of helix 5 and the actin surface (Fig. 2d), suggesting that structural rearrangements occur throughout Vt upon actin binding. To visualize this conformational transition in detail, we performed molecular dynamics flexible fitting<sup>45</sup> (MDFF) of Vt residues 917–1047 and actin to generate a pseudo-atomic model of the interface (Fig. 3a). We adapted a recently developed weighting-optimization procedure<sup>46</sup> to reduce over-fitting into our medium-resolution maps (Supplementary Fig. 3). The Vt-actin interface has been extensively probed by large-scale deletions<sup>18</sup>, scanning alanine mutagenesis<sup>47</sup>, and site-directed mutagenesis<sup>28</sup>, and our model explains the preponderance of mutations previously reported to reduce actin binding. The exception, a series of multiple alanine substitutions in H3 which caused minor (10–20%) reductions in actin binding<sup>47</sup>, could potentially indirectly affect Vt actin binding by reducing stability of the protein.

To further validate our MDFF model, we mutagenized residues that mediate putative contacts at both protomer binding sites in the context of full-length Vt (residues 879–1066) and performed co-sedimentation assays (Fig. 3b-d). Mutations at both the actin 1 interface (I1046A, R987A) and actin 2 interface (M1022A, M1005A/R1008A) resulted in modest but significant reductions in actin binding. A double mutant with substitutions at both interfaces (V1001A/R987A) demonstrated dramatically reduced actin binding, highlighting the composite nature of the interface and the importance of both binding sites for full actin engagement. This double mutation resulted in a similar reduction in actin binding to the previously reported I997A mutant (Fig. 3b, pink), to our knowledge the most potent actin-binding single point mutation reported to date<sup>28</sup>. However, I997A also affects Vt's interaction with Phosphatidylinositol 4,5-bisphosphate (PIP<sub>2</sub>)<sup>28</sup>, complicating interpretation of *in vivo* studies with this construct<sup>6; 48</sup>. Future studies will focus on the affects of our newly identified mutants on Vt-PIP<sub>2</sub> interactions, with the goal of identifying clean separation-of-function mutations. Consistent with the requirement of actin binding for Vt-mediated actin bundling, all of the point mutants resulted in a bundling defect commensurate with their binding defect (Fig. 3e, f). I1046 produced an even greater defect in actin bundling than actin binding, suggesting this residue also contributes to Vt oligomerization.

R987 contacts the DNase-binding loop (D-loop) of actin 1, a region of actin which undergoes a substantial rearrangement upon polymerization<sup>49</sup> and which has been suggested to be one of the more labile contacts in the filament<sup>50</sup>. The structure of actin in the Vt-bound filament showed minimal differences (RMSD 0.720 Å) versus an MDFF model of naked actin filaments derived from a control reconstruction in the absence of Vt (7.6Å gold-standard FSC 0.143, Fig. 2a), and both of the recently reported high-resolution F-actin structures (PDB 3j8a<sup>51</sup> / 3j8i<sup>52</sup>, Fig. 4a), with minor differences distributed evenly throughout the protein (Fig. 4b). Thus, despite interacting with both rigid and flexible regions of actin, Vt binding does not alter the structure of F-actin to an extent detectable at the resolution of our maps.

### Actin binding activates H1-mediated bundling via a steric mechanism

Superposition of the crystal structure of Vt in isolation (PDB 1QKR<sup>44</sup>) with the MDFF-derived model reveals a substantial remodeling of the H1 docking site on the Vt helical bundle (Fig. 5a, b), primarily produced by a twisting rearrangement of helices 4 and 5 relative to the remainder of the bundle (Fig. 5a, Supplementary Movie 3). This would generate clashes between large inward-facing hydrophobic residues in H1 and the rearranged hydrophobic core of Vt, necessitating the displacement of H1 for this conformational transition to occur. We infer that the energy to stabilize this rearrangement is provided by actin binding, as helix 5 clashes with actin 2 in the pre-bound conformation (Fig. 2d). Thus, we propose a model in which the need to relieve multiple clashes allosterically couples actin binding to H1 release.

Since H1 release is the largest conformational change which occurs upon Vt actin engagement, we hypothesized that H1 could play a previously unappreciated role in actin bundling. To test this hypothesis, we focused on residues which are buried in the pre-bound state, reasoning that they would either sterically promote H1 release, or mediate binding interactions in trans upon being exposed. Co-sedimentation assays demonstrated that a single point mutant of one such residue, M898A, did not significantly affect Vt actin binding in the context of full-length Vt (Fig. 5c, e), but almost completely eliminated actin bundling (Fig. 5d, f), consistent with this model. We therefore propose that H1 release upon actin binding by Vt is a key second step in vinculin activation, enabling Vt-mediated actin bundling subsequent to actin binding.

### MVt undergoes an analogous structural transition upon actin binding

We next focused our analysis on vinculin's muscle-specific splice isoform, metavinculin. We obtained an 8.2 Å reconstruction (Fig. 6a, Fig. 1d) of residues 858–1129 of human metavinculin, hereafter referred to as MVt C5, bound to F-actin. At sub-nanometer resolution, this reconstruction is essentially indistinguishable from the Vt C5 reconstruction, with minor differences in connectivity between the helical densities. In contrast to a previous negative stain reconstruction, where extra density was observed protruding from MVt when compared with Vt<sup>37</sup>, rigid-body docking of the MVt crystal structure into our sub-nanometer resolution density map demonstrates that helix H1' is also displaced from the helical bundle when MVt binds actin, in agreement with the similar proteolysis susceptibility profile reported for MVt H1' and Vt H1 upon actin binding<sup>38</sup>. In



addition to the different resolutions of the studies, an explanation for this discrepancy may lie in the different constructs used for structural analysis, as the previous reconstruction excluded residues 858–879 and included residues 1130–1134.

Additional density is also present on the surface of MVt C5 decorated filaments, forming a different pattern compared to Vt C5 (Fig. 6a). Although it is tempting to speculate that the displaced H1' forms slightly different contacts with the actin surface, higher resolution reconstructions will be required to visualize these interactions in detail. Superimposing an equivalent MDFF model of MVt-actin with that of Vt-actin (Fig. 6b) shows only minor differences in both actin (0.732 Å RMSD) and the bound protein (0.752 Å RMSD), supporting our assertion from inspection of the density maps, that at sub-nanometer resolution, the interfaces are effectively indistinguishable. Nevertheless, a recent report which demonstrated that MVt alters the mechanical properties of actin filaments included spectroscopic evidence of actin structural rearrangements in the presence of MVt<sup>38</sup>. Thus, it is possible that subtle rearrangements of individual actin residues do occur, which would require higher resolution to visualize.

### **MVt inhibits Vt-mediated actin bundling**

Although Vt is a potent actin bundling factor, MVt has previously been reported to lack this activity<sup>32; 37</sup>. Our observations that MVt H1' and Vt H1 are released upon actin binding, and that H1 mediates Vt's actin bundling activity, provide an appealing explanation: H1', which differs in sequence, fails to promote MVt dimerization upon actin engagement. Interestingly, the H1 sequence is nevertheless present in our MVt construct, suggesting that the presence of H1' inhibits the ability of released H1 to mediate MVt interactions in trans. In vivo, metavinculin is always co-expressed with vinculin, with an increasing amount of metavinculin expression positively correlating with tissue contractility<sup>53</sup>. We thus investigated the effects of the presence of MVt on Vt-mediated actin bundling.

Consistent with previous studies, we found that full-length Vt robustly produces large actin bundles (Supplementary Fig. 4a-c), which were apparent in electron micrographs of negatively-stained specimens (Supplementary Fig. 4a) and in the low speed pellet of a differential centrifugation assay (Sup Fig. 4b, c). Conversely, MVt failed to produce bundles (Supplementary Fig. 4a-c), although binding was apparent in the micrographs (Supplementary Fig. 4a) and pelleting assays (data not shown). In agreement with a recent report<sup>38</sup>, we found that varying the ratio of MVt and Vt in the context of a constant amount of total binding protein produced reduced bundling relative to Vt alone (Supplementary Fig. 4d-f). Interestingly, this effect is not attributable to simply reducing the amount of Vt, as omitting MVt under identical conditions robustly produced bundles (Supplementary. Fig. 4g, h), suggesting that one function of metavinculin is to suppress actin bundling by vinculin. We tested this hypothesis by adding increasing amounts of MVt under conditions of a constant amount of Vt (Fig. 6c, d), which mimics physiological conditions, wherein vinculin expression remains fairly constant and metavinculin expression varies<sup>53</sup>. The presence of a small amount of MVt produced a drastic reduction in actin bundling, in agreement with a model wherein MVt “poisons” the actin bundling activity of Vt<sup>38</sup>.

## Discussion

Utilizing cryo-EM, molecular modeling, and complimentary binding assays, we have produced detailed models of the critical interactions between both vinculin isoforms and F-actin. Our data support the recent DMD model of Thompson et al., in which the primary Vt actin-binding interface comprises helices 4 and 5. In addition to clarifying the literature and rationalizing the preponderance of mutations previously reported to affect the vinculin-actin interaction, our model can serve as a guide for the selection of separation-of-function mutants for future studies which seek to specifically interrogate the role of vinculin's actin-binding activity. Additionally, the data-processing strategy we have developed for visualizing this low-affinity complex can be employed to study the interaction of F-actin with other binding partners, few of which have been structurally analyzed by cryo-EM at similar resolution<sup>51; 54; 55; 56</sup>.

Our finding that helix H1 undocks from the Vt bundle upon actin engagement to mediate actin bundling, reminiscent of earlier predictions of “unfurling” of this domain<sup>44</sup>, adds an additional layer to the vinculin activation mechanism (Fig. 7). After the interaction between Vh and Vt is disrupted, H1 must also be disengaged to license the Vt-actin interaction. Although our data do not discriminate between H1 release followed by actin binding or vice-versa, the steric incompatibility between the H1-docked state and the actin-bound state, as well as NMR data suggesting that H1 undergoes conformational exchange in the isolated Vt<sup>57</sup>, support the former model. Since M898, an H1 residue that is buried in the pre-bound state, is required to support actin bundling by Vt, we conclude that this conformational transition is required for vinculin's actin-bundling activity. The structure of the actin-induced Vt dimer (reviewed in ref. <sup>58</sup>) remains an important subject for future investigations.

Vinculin sustains substantial tensile forces in adhesions *in vivo*<sup>59</sup>, and a recent super-resolution light microscopy study demonstrated that the molecule is, on average, oriented along the dorsal-ventral axis of an adherent cell with the Vh domain closer to the ventral surface<sup>48</sup>. These data suggest that a vinculin molecule bound to both talin via Vh and actin by Vt will experience tensile forces in a geometry that will favor the undocking of H1 from the Vt bundle. We speculate that this may give rise to a mechanism by which vinculin can reinforce adhesion in response to force: if H1 is in equilibrium between the docked and undocked states, the presence of tension will favor H1 undocking, and by extension vinculin actin binding and bundling, bolstering the adhesion-cytoskeleton linkage (Fig. 7).

Our finding that MVt suppresses actin bundling by Vt suggests that one role of metavinculin is to tune actin bundling by vinculin in highly contractile tissues, the physiological significance of which is an important subject for future investigation. The detailed molecular mechanism for this inhibition, as well as that underlying Vt oligomerization to bundle actin, remain to be determined. When removed from the context of Vt, the sequence comprising H1 fused to GFP fails to dimerize, does not interact with the Vt-actin complex, and does not interact with actin (data not shown). Our mass-tagging experiments (Fig. 2b) demonstrating that the undocked H1 segment and the Vt C-terminus are closely apposed on the actin surface, as well as the previous demonstration that the Vt C-terminus is required for



bundling<sup>27</sup>, lead us to speculate that bringing these two segments into close spatial proximity contributes to the generation of the Vt oligomerization interface.

The metavinculin insertion fused to GFP similarly does not suppress Vt-mediated actin bundling (data not shown), although it does in the context of actin bound MVt, where H1' is also released. Additionally, H1' was reported to be dispensable for Vt-MVt interaction in presence of PIP<sub>2</sub> and the absence of actin<sup>36</sup>. These data are most consistent with the recent proposal that the negative charge of the metavinculin insertion, which is highly acidic, inhibits actin bundling through electrostatic repulsion, as the released H1' would allow this negative charge to sample a large volume while remaining tethered to the actin-bound MVt<sup>38</sup>. However, this model is difficult to reconcile with the observation that single disease point mutations in MVt result in actin aggregation by this domain in vitro<sup>32</sup>, supporting a more specific inhibitory role for this segment in the actin-bound context. This suggests a complex interplay between the ordered and disordered regions of these proteins on the actin surface that cannot be easily dissected through primary structure-function analysis. By precisely defining these regions, their poses and conformations on actin, and the activities they confer, this study paves the way to delineating the mechanisms at work.

## Methods

### Expression Cloning

The C-terminally GFP tagged construct (Vt C5-GFP, Vt residues 879–1061 with a C-terminal GFP fusion linked by the sequence “GIGSGSNGSSGS”) was generated using Ligation Independent Cloning (LIC) in the H6-msfGFP vector (Addgene #29725), which encodes an N-terminal, TEV cleavable hexa-histidine tag, the linker, and a C-terminal EGFP tag. The N-terminally tagged construct (GFP-E892-Vt C5, Vt residues 892–1061 with an N-terminal GFP fusion and no linker sequence) was generated using Sequence and Ligation Independent Cloning (SLIC), inserting the ORF in-frame after the GFP. The codon-optimized sequence of human MVt (residues 858–1134) for bacterial expression was synthesized (Geneart), and MVt and MVt C5 (residues 858–1129) were subcloned into the 2HR-T vector (Addgene #29718), which encodes an N-terminal, TEV cleavable hexa-histidine tag, using LIC.

### Protein Purification

The full length Vt constructs employed in pelleting assays and negative stain-EM experiments (comprising chicken vinculin amino acids 879–1066) and Vt C5 construct employed for cryo-EM structure determination (comprising chicken vinculin amino acids 879–1061) were expressed and purified as previously reported<sup>27</sup>. Rabbit muscle actin was purified as previously described<sup>60</sup>. MVt, MVt C5, and Vt C5 GFP-fusion constructs were expressed in BL21(DE3)-Rosetta 2 cells. Expression was induced with 0.5 mM IPTG, followed by overnight shaking at 25°C. Cells were harvested at 5,000 RCF, then lysed by sonic disruption in Lysis Buffer (50 mM Tris-Cl, 200 mM NaCl, 10 mM imidazole, 5 mM beta-mercaptoethanol, pH 8.0) supplemented with Complete ULTRA protease inhibitor tablets (Roche). Lysates were clarified by centrifugation at 20,000 RCF, and the fusion proteins then captured by batch binding to Ni-NTA resin (Qiagen). The resin was poured

into a gravity column, then washed with 20 column volumes Wash Buffer (50 mM Tris-Cl, 200 mM NaCl, 25 mM imidazole, 5 mM beta-mercaptoethanol, pH 8.0), and eluted with 10 column volumes of Elution Buffer (50 mM Tris-Cl, 200 mM NaCl, 250 mM imidazole, 5 mM beta-mercaptoethanol, pH 8.0). The hexa-histidine tag was cleaved with TEV protease (1:50 w/w ratio) during overnight dialysis against Storage Buffer (25mM Tris-Cl pH 8.0, 150 mM NaCl, 1 mM EDTA, 1 mM DTT) at 4°C. The cleaved protein was then purified by size exclusion chromatography using a Superdex 200 Increase column (GE Healthcare) pre-equilibrated with Storage Buffer. Peak fractions were pooled, concentrated by ultrafiltration, and flash-frozen in liquid nitrogen.

### Cryo-EM sample preparation

F-actin and Vt C5 / MVt C5 constructs were diluted to 0.3  $\mu\text{M}$  and 10  $\mu\text{M}$ , respectively, in KMEI (50 mM KCl, 1 mM  $\text{MgCl}_2$ , 1 mM EGTA, 10 mM imidazole, pH 7.0). 3  $\mu\text{l}$  of actin was applied to a plasma-cleaned 1.2 / 1.3 200 mesh C-flat holey carbon grid (Protochips) in the humidified chamber of a Leica GP plunge freezer and incubated for 60s at 25°C. 3  $\mu\text{l}$  of binding protein was then applied and incubated for 60 s. 3  $\mu\text{l}$  of solution was then removed and an additional 3  $\mu\text{l}$  of vinculin applied. After an additional 60 s, 3  $\mu\text{l}$  of solution was removed, then the grid was blotted for 2 s and plunge-frozen in liquid ethane.

### Cryo-EM data collection

Cryo-EM data were collected with the Legicon software package<sup>61</sup> on a Tecnai F20 operating at 120 kV using a Gatan Ultrascan 4K CCD. Images were collected with a dose of 25 electrons /  $\text{\AA}^2$  and underfocus ranging from 1.5 to 3 microns at 100,000 X magnification, corresponding to a calibrated pixel size of 1.09  $\text{\AA}$  at the specimen level.

### 2D Image processing

Contrast transfer function (CTF) estimation and extraction of segments was performed in the Appion data processing environment<sup>62</sup>. Unless otherwise noted, operations were carried out using proc2d from the EMAN processing package<sup>63</sup>. CTF parameters were estimated with CTFFIND3<sup>64</sup>. Segments were windowed in 512 pixel boxes with 81  $\text{\AA}$  of non-overlap, corresponding to a step-size of 3 actin protomers, normalized with xmipp\_normalize<sup>65</sup>, then binned by 2. Reference-free two-dimensional classification and averaging was performed with RELION 1.3<sup>66</sup>. For 3D reconstruction with SPARX/EMAN2, segments were extracted from phase-flipped images. For 2D classification with RELION and 3D reconstruction with FREALIGN, CTF correction was performed internally.

### 3D sorting

We adapted an image processing procedure previously developed for reconstructing microtubule specimens for this work, which implements the Iterative Helical Real Space Refinement protocol<sup>39</sup>. Refinement and reconstruction is performed using functions from the EMAN2/SPARX libraries<sup>41; 42</sup>, and the helical search is performed using the program hsearch\_lorentz of Egelman<sup>39</sup>. Segments which contributed to featureful 2D class-averages were used for 3D refinement. An initial model was generated by low-pass filtering an actin reconstruction (EMD-1990<sup>54</sup>) to 35  $\text{\AA}$ . Initially a single-model 3D refinement was

performed using all segments from the Vt C5-F-actin dataset. This produced a reconstruction in which the Vt density was clearly sub-stoichiometric, suggesting that sorting bound from unbound segments would improve the reconstruction.

We collected a dataset of naked F-actin filaments and performed a single-model refinement as described above. We then used the sub-stoichiometric Vt C5-F-actin and naked F-actin models, both low-pass filtered at 35 Å, to perform a multi-model 3D refinement. Segments were also excluded from the reconstructions based on a cross-correlation cutoff. Several iterations of this procedure produced a Vt C5-bound model with substantially improved occupancy: we selected the segments which contributed to this model for further refinement.

### Independent half-map refinement

Refining datasets in independent halves has recently been introduced as a standard to reduce over-fitting and improving resolution estimates by the Fourier Shell Correlation (FSC)<sup>67</sup>. We developed a single-model IHRSR implementation of this so-called “gold-standard FSC” based refinement using our EMAN2/SPARX procedure. Segments selected by the multi-model procedure were divided into random half-datasets. The same low-pass filtered initial reference was used for each half-dataset. After each round of refinement, the asymmetric reconstructions of the half-datasets were summed, and the sum used to calculate new helical parameters. These helical parameters were then applied to each half-reconstruction independently, which were then compared and low-pass filtered based on the FSC to provide the references for the next round of refinement. This procedure maintains independent noise between the two half-datasets, while anchoring them to have the same helical parameters which are iteratively refined. Further segments were not excluded by a cross-correlation cutoff at this stage of refinement.

After refinement in EMAN2/SPARX, final refinement and CTF-corrected reconstruction was performed using FREALIGN v9.03<sup>43</sup> with fixed helical parameters from the final round of IHRSR. The half-datasets were independently refined and reconstructed, and a single merged reconstruction was also generated using the alignment parameters from the independent halves. The data from the GFP-Vt and MVt constructs were processed using an identical procedure; for the naked F-actin dataset only a single model was used for the first stage of refinement.

All software is available upon request.

### Post-processing

The final resolutions of the Vt C5-F-actin, MVt C5-F-actin, and naked F-actin reconstructions were 8.5, 8.2, and 7.6 Å, respectively, based on the FSC 0.143 criterion. The maps were amplitude-sharpened using the program BFACTOR (<http://grioriefflab.janelia.org/bfactor>), with a negative B-factor of -1000, -1000, and -750 Å<sup>3</sup>, respectively, with the high-frequency cutoff determined by the FSC 0.143. Difference maps were calculated between the GFP-Vt reconstructions and the Vt C5 reconstruction using the program DIFFMAP (<http://grioriefflab.janelia.org/diffmap>), with unsharpened maps as inputs, then low-pass filtered to 15 Å prior to visualization.

## Molecular Dynamics Flexible Fitting

In order to aid the interpretation of our maps, we utilized the molecular dynamics flexible fitting procedure (MDFF)<sup>45</sup>. In this and related procedures, the weighting between the experimental cryo-EM map and the model parameters (in this case the molecular dynamics force-field) must be carefully chosen to take full advantage of the experimental data while avoiding the pitfall of over-fitting due to limited resolution and noise in the reconstruction.

To this end we implemented the protocol recently proposed by DiMaio and co-workers, which makes use of independent half-maps to optimize the weighting parameter  $g$ <sup>46</sup>. The half-maps from the Vt C5-F-actin reconstruction and F-actin alone reconstruction were B-factor sharpened identically to the corresponding full reconstruction. Rigid-body docking models were then generated from a segment of the Vt crystal structure (PDB 1QKR<sup>44</sup>) corresponding to residues 917–1047 and the recently reported high-resolution cryo-EM structure of F-actin bound to tropomyosin (PDB 3J8A<sup>51</sup>) using UCSF Chimera. The model consisted of 8 actin protomers and 6 Vt molecules, producing a central layer of the model where all protein-protein interactions are satisfied. To generate the starting model for human MVt, residue 943 of the Vt model was computationally mutagenized from asparagine to threonine using UCSF Chimera<sup>68</sup>, the only difference in sequence between the two constructs.

MDFF simulations were then performed varying  $g$  with explicit solvent and 50 mM KCl. After a brief energy minimization step to remove severe clashes from the starting model, the recommended MDFF procedure proceeds in two steps: molecular dynamics with a low-map weighting, and a final longer energy minimization using a high map-weighting. We attempted varying  $g$  at both steps, and varying  $g$  at the second step while keeping a constant recommended value of 0.3 at the first step (Supplementary Figure 5). Model fitting (100 ns simulation followed by 2000 minimization steps) was performed with one of the two half-maps (the “training map”), then compared to the high resolution shells of the other half-map (the “test map”) via the FSC, which has been found to be more sensitive to over-fitting than real-space correlation<sup>46</sup>. Model quality was also assessed using MolProbity<sup>69</sup> as implemented in Phenix<sup>70</sup>. Overfitting was detected by a divergence in the FSC between the training map and the half-map, which corresponded to a deterioration in the model quality as assessed by MolProbity.

Final MDFF models were generated using the full reconstructions (250 ns simulation, 2000 minimization steps). Symmetry restraints were imposed on the C $\alpha$  atoms of the actin protomers as described, and the positions of bound ADP and Magnesium ions were kept fixed during the molecular dynamics step due to the limited resolution of the reconstructions.

## Negative stain EM

Actin, full-length Vt, and full-length MVt were mixed in KMEI in the indicated ratios and incubated for 15 minutes. 4  $\mu$ l of sample was applied to a glow-discharged continuous carbon grid (Ted Pella). After 60 s of incubation, the grid was washed in 3 100  $\mu$ l drops of

1% uranyl acetate and blotted to dryness. Images were collected on a FEI Tecnai 12 operating at 120 kV using an Ultrascan 2K CCD camera (Gatan).

### Actin Co-sedimentation assays

Actin co-sedimentation assays in Figures 2 and 3, and Supplementary Figures 3 and 4, were performed as previously reported<sup>27; 28</sup>. All co-sedimentation assays were performed with constructs comprising full-length Vt (residues 879–1066) and MVt (residues 858–1134). Briefly, actin-Vt mixtures were generated to the concentrations reported (10  $\mu$ M Vt, variable actin concentrations) and were incubated at room temperature for 30 minutes in co-sedimentation buffer (10 mM Tris pH 7.5, 100 mM KCl, 2.5 mM MgCl<sub>2</sub>, and 2 mM dithiothreitol (DTT)). The samples were then spun for 30 min at 150,000 RCF and the supernatant and pellet separated. These fractions were resuspended to equal volumes and analyzed by SDS PAGE. For actin binding, the density of the Vt band was determined and the percentage of Vt in the pelleted fraction was determined. For actin bundling, 20  $\mu$ M F-actin was used instead of various concentrations. The samples were spun for 10 minutes at 5,000 RCF and the supernatant and pellet fractions separated. After SDS PAGE analysis, densitometry was performed with ImageJ<sup>71</sup>.

Co-sedimentation assays in Fig. 6 and Supplementary Fig. 6 were performed as stated above, with the following changes: For actin bundling, 3 $\mu$ M F-actin was mixed with the indicated concentrations of Vt and/or MVt, in KMEI buffer. The samples were spun for 15 minutes at 12,000 RCF and the supernatant and pellet fractions collected. The supernatant fraction was then spun for 15 min at 350,000 RCF and the supernatant and pellet fractions collected. The pellet from the first step (low-speed pellet) and pellet from the second step (high-speed pellet) were resuspended in an equal volume to the supernatant, followed by analysis by SDS-PAGE.

### Molecular Graphics

All display items were prepared using UCSF Chimera<sup>68</sup>, which was also used for segmenting maps and superimposing atomic models. Density map coloring in Figure 2b and Figure 6a was assigned by a 4.5 Å distance cutoff from docked atomic models and bead models of unoccupied densities. Reported RMSD values for actin correspond to superpositions of Chain A in the deposited MDFF models. Electrostatic potential surface map was calculated with the Adaptive Poisson-Boltzmann Solver (APBS)<sup>72</sup>.

### Statistics

Student's t-tests were performed using Microsoft excel.

### Supplementary Material

Refer to Web version on PubMed Central for supplementary material.

### Acknowledgements

We gratefully acknowledge Jenny Hinshaw, NIDDK, for the use of her Tecnai F20 electron microscope, Alisdair Steven, NIAID for use of his vitrification apparatus, and Scott Gradia, UC Berkeley, for the generation and

deposition of expression vectors in Addgene. We thank Yasuharu Takagi and James Sellers, NHLBI, for the gift of rabbit muscle actin. We also acknowledge Eva Nogales, UC Berkeley, for use of computational resources during the early stages of this project. This study utilized the high-performance Biowulf Linux cluster (<http://biowulf.nih.gov>). We also gratefully acknowledge Robert Cail, NHLBI, for generating the Vt C5-GFP construct and Pinar Gurel, NHLBI, for critical reading of the manuscript. This work was supported by an NIH Director's Early Independence Award (1DP5OD17885-1) to G.M.A. and the NHLBI Division of Intramural Research.

## References

1. Peng X, Nelson ES, Maiers JL, DeMali KA. New insights into vinculin function and regulation. *Int Rev Cell Mol Biol.* 2011; 287:191–231. [PubMed: 21414589]
2. Carisey A, Ballestrem C. Vinculin, an adapter protein in control of cell adhesion signalling. *Eur J Cell Biol.* 2011; 90:157–163. [PubMed: 20655620]
3. Parsons JT, Horwitz AR, Schwartz MA. Cell adhesion: integrating cytoskeletal dynamics and cellular tension. *Nat Rev Mol Cell Biol.* 2010; 11:633–643. [PubMed: 20729930]
4. Diez G, Auernheimer V, Fabry B, Goldmann WH. Head/tail interaction of vinculin influences cell mechanical behavior. *Biochem Biophys Res Commun.* 2011; 406:85–88. [PubMed: 21295550]
5. Plotnikov SV, Sabass B, Schwarz US, Waterman CM. High-resolution traction force microscopy. *Methods Cell Biol.* 2014; 123:367–394. [PubMed: 24974038]
6. Thievensen I, Thompson PM, Berlemont S, Plevock KM, Plotnikov SV, Zemljic-Harpf A, Ross RS, Davidson MW, Danuser G, Campbell SL, Waterman CM. Vinculin-actin interaction couples actin retrograde flow to focal adhesions, but is dispensable for focal adhesion growth. *J Cell Biol.* 2013; 202:163–177. [PubMed: 23836933]
7. Riveline D, Zamir E, Balaban NQ, Schwarz US, Ishizaki T, Narumiya S, Kam Z, Geiger B, Bershadsky AD. Focal contacts as mechanosensors: externally applied local mechanical force induces growth of focal contacts by an mDia1-dependent and ROCK-independent mechanism. *J Cell Biol.* 2001; 153:1175–1186. [PubMed: 11402062]
8. Dumbauld DW, Lee TT, Singh A, Scrimgeour J, Gersbach CA, Zamir EA, Fu J, Chen CS, Curtis JE, Craig SW, Garcia AJ. How vinculin regulates force transmission. *Proc Natl Acad Sci U S A.* 2013; 110:9788–9793. [PubMed: 23716647]
9. Saunders RM, Holt MR, Jennings L, Sutton DH, Barsukov IL, Bobkov A, Liddington RC, Adamson EA, Dunn GA, Critchley DR. Role of vinculin in regulating focal adhesion turnover. *Eur J Cell Biol.* 2006; 85:487–500. [PubMed: 16584805]
10. Carisey A, Tsang R, Greiner AM, Nijenhuis N, Heath N, Nazgiewicz A, Kemkemer R, Derby B, Spatz J, Ballestrem C. Vinculin regulates the recruitment and release of core focal adhesion proteins in a force-dependent manner. *Curr Biol.* 2013; 23:271–281. [PubMed: 23375895]
11. Xu W, Baribault H, Adamson ED. Vinculin knockout results in heart and brain defects during embryonic development. *Development.* 1998; 125:327–337. [PubMed: 9486805]
12. Bakolitsa C, Cohen DM, Bankston LA, Bobkov AA, Cadwell GW, Jennings L, Critchley DR, Craig SW, Liddington RC. Structural basis for vinculin activation at sites of cell adhesion. *Nature.* 2004; 430:583–586. [PubMed: 15195105]
13. Winkler J, Lunsdorf H, Jockusch BM. The ultrastructure of chicken gizzard vinculin as visualized by high-resolution electron microscopy. *J Struct Biol.* 1996; 116:270–277. [PubMed: 8812983]
14. Borgon RA, Vornrhein C, Bricogne G, Bois PR, Izard T. Crystal structure of human vinculin. *Structure.* 2004; 12:1189–1197. [PubMed: 15242595]
15. Burridge K, Mangeat P. An interaction between vinculin and talin. *Nature.* 1984; 308:744–746. [PubMed: 6425696]
16. Groesch ME, Otto JJ. Purification and characterization of an 85 kDa talin-binding fragment of vinculin. *Cell Motil Cytoskeleton.* 1990; 15:41–50. [PubMed: 2104778]
17. Jockusch BM, Isenberg G. Interaction of alpha-actinin and vinculin with actin: opposite effects on filament network formation. *Proc Natl Acad Sci U S A.* 1981; 78:3005–3009. [PubMed: 6789327]
18. Huttelmaier S, Bubeck P, Rudiger M, Jockusch BM. Characterization of two F-actin-binding and oligomerization sites in the cell-contact protein vinculin. *Eur J Biochem.* 1997; 247:1136–1142. [PubMed: 9288940]



19. Chen H, Cohen DM, Choudhury DM, Kioka N, Craig SW. Spatial distribution and functional significance of activated vinculin in living cells. *J Cell Biol.* 2005; 169:459–470. [PubMed: 15883197]
20. Johnson RP, Craig SW. An intramolecular association between the head and tail domains of vinculin modulates talin binding. *J Biol Chem.* 1994; 269:12611–12619. [PubMed: 8175670]
21. Johnson RP, Craig SW. F-actin binding site masked by the intramolecular association of vinculin head and tail domains. *Nature.* 1995; 373:261–264. [PubMed: 7816144]
22. Chen H, Choudhury DM, Craig SW. Coincidence of actin filaments and talin is required to activate vinculin. *J Biol Chem.* 2006; 281:40389–40398. [PubMed: 17074767]
23. Fillingham I, Gingras AR, Papagrigoriou E, Patel B, Emsley J, Critchley DR, Roberts GC, Barsukov IL. A vinculin binding domain from the talin rod unfolds to form a complex with the vinculin head. *Structure.* 2005; 13:65–74. [PubMed: 15642262]
24. del Rio A, Perez-Jimenez R, Liu R, Roca-Cusachs P, Fernandez JM, Sheetz MP. Stretching single talin rod molecules activates vinculin binding. *Science.* 2009; 323:638–641. [PubMed: 19179532]
25. Bachir AI, Zareno J, Moissoglu K, Plow EF, Gratton E, Horwitz AR. Integrin-associated complexes form hierarchically with variable stoichiometry in nascent adhesions. *Curr Biol.* 2014; 24:1845–1853. [PubMed: 25088556]
26. Janssen ME, Kim E, Liu H, Fujimoto LM, Bobkov A, Volkmann N, Hanein D. Three-dimensional structure of vinculin bound to actin filaments. *Mol Cell.* 2006; 21:271–281. [PubMed: 16427016]
27. Shen K, Tolbert CE, Guilluy C, Swaminathan VS, Berginski ME, Burrige K, Superfine R, Campbell SL. The vinculin C-terminal hairpin mediates F-actin bundle formation, focal adhesion, and cell mechanical properties. *J Biol Chem.* 2011; 286:45103–45115. [PubMed: 22052910]
28. Thompson PM, Tolbert CE, Shen K, Kota P, Palmer SM, Plevock KM, Orlova A, Galkin VE, Burrige K, Egelman EH, Dokholyan NV, Superfine R, Campbell SL. Identification of an actin binding surface on vinculin that mediates mechanical cell and focal adhesion properties. *Structure.* 2014; 22:697–706. [PubMed: 24685146]
29. Jannie KM, Ellerbroek SM, Zhou DW, Chen S, Crompton DJ, Garcia AJ, DeMali KA. Vinculin-dependent actin bundling regulates cell migration and traction forces. *Biochem J.* 2015; 465:383–393. [PubMed: 25358683]
30. Johnson RP, Craig SW. Actin activates a cryptic dimerization potential of the vinculin tail domain. *J Biol Chem.* 2000; 275:95–105. [PubMed: 10617591]
31. Palmer SM, Schaller MD, Campbell SL. Vinculin tail conformation and self-association is independent of pH and H906 protonation. *Biochemistry.* 2008; 47:12467–12475. [PubMed: 18980387]
32. Olson TM, Illenberger S, Kishimoto NY, Huttelmaier S, Keating MT, Jockusch BM. Metavinculin mutations alter actin interaction in dilated cardiomyopathy. *Circulation.* 2002; 105:431–437. [PubMed: 11815424]
33. Maeda M, Holder E, Lowes B, Valent S, Bies RD. Dilated cardiomyopathy associated with deficiency of the cytoskeletal protein metavinculin. *Circulation.* 1997; 95:17–20. [PubMed: 8994410]
34. Vasile VC, Will ML, Ommen SR, Edwards WD, Olson TM, Ackerman MJ. Identification of a metavinculin missense mutation, R975W, associated with both hypertrophic and dilated cardiomyopathy. *Mol Genet Metab.* 2006; 87:169–174. [PubMed: 16236538]
35. Meyer T, Brink U, Unterberg C, Stohr S, Kreuzer H, Buchwald AB. Expression of meta-vinculin in human coronary arteriosclerosis is related to the histological grade of plaque formation. *Atherosclerosis.* 1994; 111:111–119. [PubMed: 7840806]
36. Rangarajan ES, Lee JH, Yogesha SD, IZard T. A helix replacement mechanism directs metavinculin functions. *PLoS One.* 2010; 5:e10679. [PubMed: 20502710]
37. Janssen ME, Liu H, Volkmann N, Hanein D. The C-terminal tail domain of metavinculin, vinculin's splice variant, severs actin filaments. *J Cell Biol.* 2012; 197:585–593. [PubMed: 22613835]
38. Oztug Durer ZA, McGillivray RM, Kang H, Elam WA, Vizcarra CL, Hanein D, De La Cruz EM, Reisler E, Quinlan ME. Metavinculin tunes the flexibility and the architecture of vinculin induced bundles of actin filaments. *J Mol Biol.* 2015

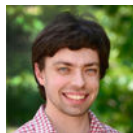
39. Egelman EH. The iterative helical real space reconstruction method: surmounting the problems posed by real polymers. *J Struct Biol.* 2007; 157:83–94. [PubMed: 16919474]
40. Alushin GM, Lander GC, Kellogg EH, Zhang R, Baker D, Nogales E. High-resolution microtubule structures reveal the structural transitions in alphabeta-tubulin upon GTP hydrolysis. *Cell.* 2014; 157:1117–1129. [PubMed: 24855948]
41. Hohn M, Tang G, Goodyear G, Baldwin PR, Huang Z, Penczek PA, Yang C, Glaeser RM, Adams PD, Ludtke SJ. SPARX, a new environment for Cryo-EM image processing. *J Struct Biol.* 2007; 157:47–55. [PubMed: 16931051]
42. Tang G, Peng L, Baldwin PR, Mann DS, Jiang W, Rees I, Ludtke SJ. EMAN2: an extensible image processing suite for electron microscopy. *J Struct Biol.* 2007; 157:38–46. [PubMed: 16859925]
43. Lyumkis D, Brilot AF, Theobald DL, Grigorieff N. Likelihood-based classification of cryo-EM images using FREALIGN. *J Struct Biol.* 2013; 183:377–388. [PubMed: 23872434]
44. Bakolitsa C, de Pereda JM, Bagshaw CR, Critchley DR, Liddington RC. Crystal structure of the vinculin tail suggests a pathway for activation. *Cell.* 1999; 99:603–613. [PubMed: 10612396]
45. Trabuco LG, Villa E, Mitra K, Frank J, Schulten K. Flexible fitting of atomic structures into electron microscopy maps using molecular dynamics. *Structure.* 2008; 16:673–683. [PubMed: 18462672]
46. DiMaio F, Zhang J, Chiu W, Baker D. Cryo-EM model validation using independent map reconstructions. *Protein Sci.* 2013; 22:865–868. [PubMed: 23592445]
47. Cohen DM, Chen H, Johnson RP, Choudhury B, Craig SW. Two distinct head-tail interfaces cooperate to suppress activation of vinculin by talin. *J Biol Chem.* 2005; 280:17109–17117. [PubMed: 15728584]
48. Case LB, Baird MA, Shtengel G, Campbell SL, Hess HF, Davidson MW, Waterman CM. Molecular mechanism of vinculin activation and nanoscale spatial organization in focal adhesions. *Nat Cell Biol.* 2015; 17:880–892. [PubMed: 26053221]
49. Otterbein LR, Graceffa P, Dominguez R. The crystal structure of uncomplexed actin in the ADP state. *Science.* 2001; 293:708–711. [PubMed: 11474115]
50. Galkin VE, Orlova A, Schroder GF, Egelman EH. Structural polymorphism in F-actin. *Nat Struct Mol Biol.* 2010; 17:1318–1323. [PubMed: 20935633]
51. von der Ecken J, Muller M, Lehman W, Manstein DJ, Penczek PA, Raunser S. Structure of the F-actin-tropomyosin complex. *Nature.* 2015; 519:114–117. [PubMed: 25470062]
52. Galkin VE, Orlova A, Vos MR, Schroder GF, Egelman EH. Near-atomic resolution for one state of f-actin. *Structure.* 2015; 23:173–182. [PubMed: 25533486]
53. Belkin AM, Ornatsky OI, Kabakov AE, Glukhova MA, Koteliansky VE. Diversity of vinculin/meta-vinculin in human tissues and cultivated cells. Expression of muscle specific variants of vinculin in human aorta smooth muscle cells. *J Biol Chem.* 1988; 263:6631–6635. [PubMed: 3129429]
54. Behrmann E, Muller M, Penczek PA, Mannherz HG, Manstein DJ, Raunser S. Structure of the rigor actin-tropomyosin-myosin complex. *Cell.* 2012; 150:327–338. [PubMed: 22817895]
55. Galkin VE, Orlova A, Kudryashov DS, Solodukhin A, Reisler E, Schroder GF, Egelman EH. Remodeling of actin filaments by ADF/cofilin proteins. *Proc Natl Acad Sci U S A.* 2011; 108:20568–20572. [PubMed: 22158895]
56. Ge P, Durer ZA, Kudryashov D, Zhou ZH, Reisler E. Cryo-EM reveals different coronin binding modes for ADP- and ADP-BeFx actin filaments. *Nat Struct Mol Biol.* 2014; 21:1075–1081. [PubMed: 25362487]
57. Palmer SM, Campbell SL. Backbone 1H, 13C, and 15N NMR assignments of the tail domain of vinculin. *Biomol NMR Assign.* 2008; 2:69–71. [PubMed: 19636928]
58. Thompson PM, Tolbert CE, Campbell SL. Vinculin and metavinculin: oligomerization and interactions with F-actin. *FEBS Lett.* 2013; 587:1220–1229. [PubMed: 23466368]
59. Grashoff C, Hoffman BD, Brenner MD, Zhou R, Parsons M, Yang MT, McLean MA, Sligar SG, Chen CS, Ha T, Schwartz MA. Measuring mechanical tension across vinculin reveals regulation of focal adhesion dynamics. *Nature.* 2010; 466:263–266. [PubMed: 20613844]

60. Pardee JD, Spudich JA. Purification of muscle actin. *Methods Cell Biol.* 1982; 24:271–289. [PubMed: 7098993]
61. Suloway C, Pulokas J, Fellmann D, Cheng A, Guerra F, Quispe J, Stagg S, Potter CS, Carragher B. Automated molecular microscopy: the new Legimin system. *J Struct Biol.* 2005; 151:41–60. [PubMed: 15890530]
62. Lander GC, Stagg SM, Voss NR, Cheng A, Fellmann D, Pulokas J, Yoshioka C, Irving C, Mulder A, Lau PW, Lyumkis D, Potter CS, Carragher B. Appion: an integrated, database-driven pipeline to facilitate EM image processing. *J Struct Biol.* 2009; 166:95–102. [PubMed: 19263523]
63. Ludtke SJ, Baldwin PR, Chiu W. EMAN: semiautomated software for high-resolution single-particle reconstructions. *J Struct Biol.* 1999; 128:82–97. [PubMed: 10600563]
64. Mindell JA, Grigorieff N. Accurate determination of local defocus and specimen tilt in electron microscopy. *J Struct Biol.* 2003; 142:334–347. [PubMed: 12781660]
65. Scheres SH, Nunez-Ramirez R, Sorzano CO, Carazo JM, Marabini R. Image processing for electron microscopy single-particle analysis using XMIPP. *Nat Protoc.* 2008; 3:977–990. [PubMed: 18536645]
66. Scheres SH. RELION: implementation of a Bayesian approach to cryo-EM structure determination. *J Struct Biol.* 2012; 180:519–530. [PubMed: 23000701]
67. Scheres SH, Chen S. Prevention of overfitting in cryo-EM structure determination. *Nat Methods.* 2012; 9:853–854. [PubMed: 22842542]
68. Pettersen EF, Goddard TD, Huang CC, Couch GS, Greenblatt DM, Meng EC, Ferrin TE. UCSF Chimera—a visualization system for exploratory research and analysis. *J Comput Chem.* 2004; 25:1605–1612. [PubMed: 15264254]
69. Davis IW, Leaver-Fay A, Chen VB, Block JN, Kapral GJ, Wang X, Murray LW, Arendall WB 3rd, Snoeyink J, Richardson JS, Richardson DC. MolProbity: all-atom contacts and structure validation for proteins and nucleic acids. *Nucleic Acids Res.* 2007; 35:W375–W383. [PubMed: 17452350]
70. Adams PD, Afonine PV, Bunkoczi G, Chen VB, Davis IW, Echols N, Headd JJ, Hung LW, Kapral GJ, Grosse-Kunstleve RW, McCoy AJ, Moriarty NW, Oeffner R, Read RJ, Richardson DC, Richardson JS, Terwilliger TC, Zwart PH. PHENIX: a comprehensive Python-based system for macromolecular structure solution. *Acta Crystallogr D Biol Crystallogr.* 2010; 66:213–221. [PubMed: 20124702]
71. Schneider CA, Rasband WS, Eliceiri KW. NIH Image to ImageJ: 25 years of image analysis. *Nat Methods.* 2012; 9:671–675. [PubMed: 22930834]
72. Baker NA, Sept D, Joseph S, Holst MJ, McCammon JA. Electrostatics of nanosystems: application to microtubules and the ribosome. *Proc Natl Acad Sci U S A.* 2001; 98:10037–10041. [PubMed: 11517324]

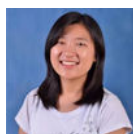
## Biographies



Laura Kim



Peter M. Thompson



Hyunna T. Lee



Sharon L. Campbell



Gregory M. Alushin

**Highlights**

- 1) Cryo-EM reconstructions of vinculin (Vt) and metavinculin (MVt) tail domains bound to F-actin.
- 2) MVt and Vt undergo partial unfolding transitions upon actin engagement.
- 3) This partial unfolding transition is required for actin bundling by Vt.
- 4) Tension will favor the partially unfolded, actin bound state, reinforcing adhesion through vinculin.

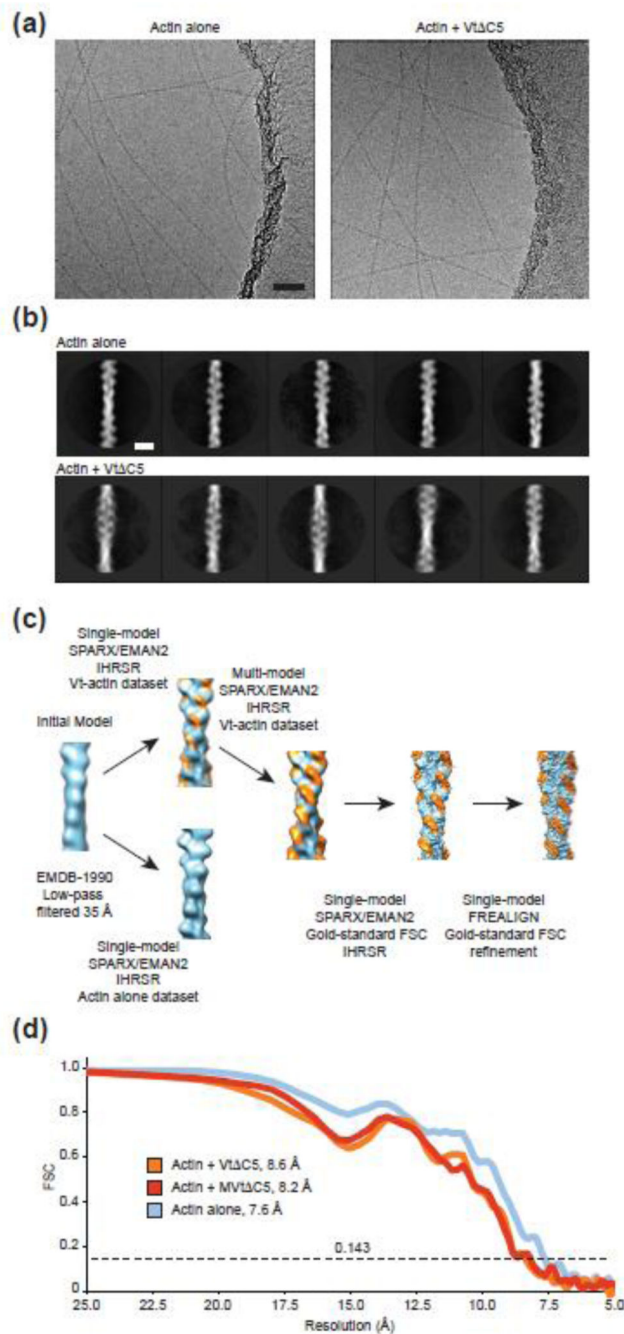


### Figure 1. Cryo-EM of the Vt-actin interface

(a) Cryo-EM micrographs of actin filaments in the presence (right) and absence (left) of Vt C5. Bar, 50 nm. (b) Reference-free class averages of segments extracted from the indicated datasets. Clear density for Vt is not readily discernible. Bar, 10 nm. (c) Overview of the multi-model reconstruction strategy to visualize substoichiometric Vt C5. Actin, light blue, Vt C5, orange. (d) Fourier Shell Correlation curves of independently-reconstructed half reconstructions (“gold-standard”) for the indicated specimens.



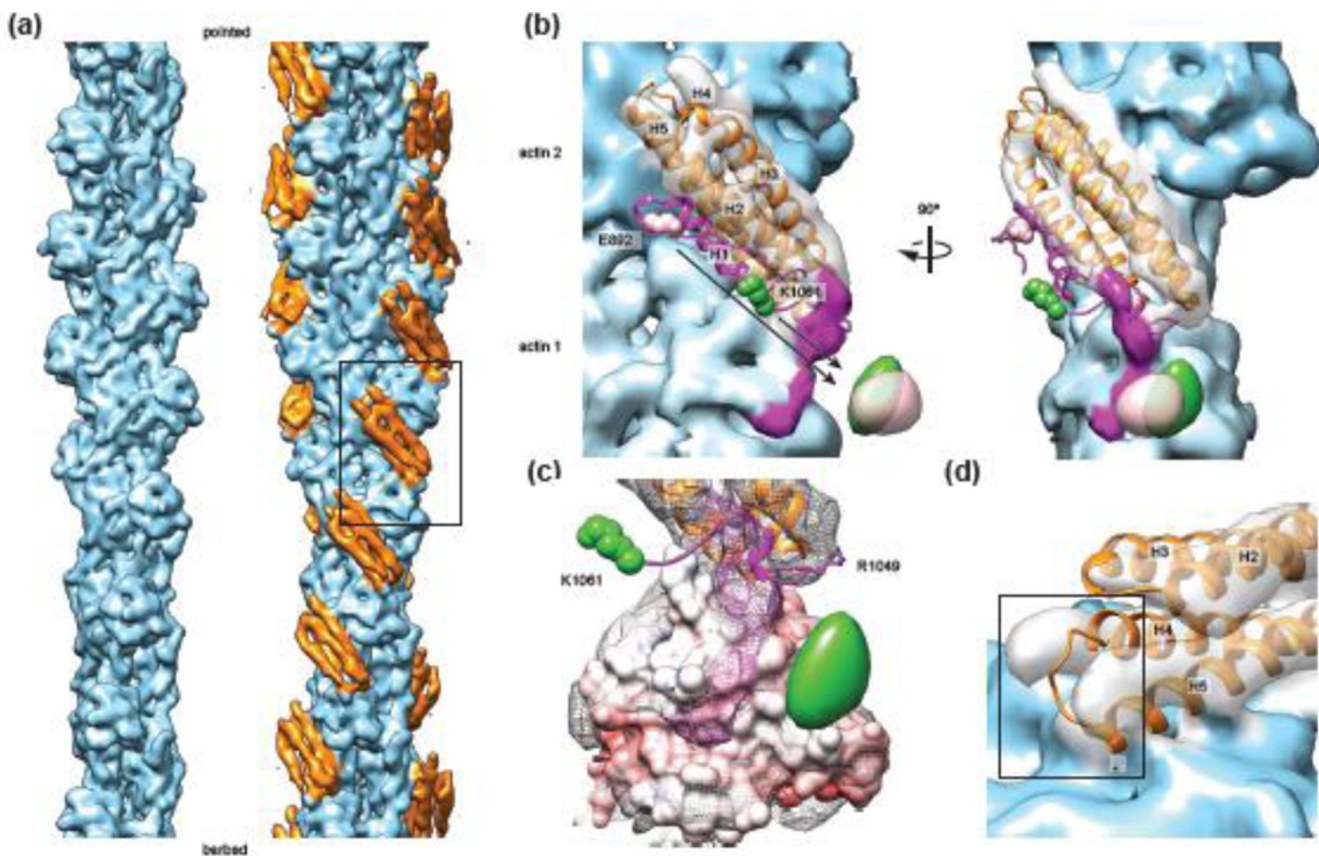


**Figure 2. Subnanometer-resolution reconstruction of the Vt-actin interface**

(a) Reconstructions of actin alone (left) and actin decorated with Vt C5 (right). Actin, light blue, Vt, orange. (b) Rigid-body docking of the Vt crystal structure. Helix 1 (H1), which was not visualized, is colored magenta. Cryo-EM density attributed to actin and Vt by docking analysis are colored blue and transparent grey, respectively. Difference maps of GFP-E892-Vt C5 – Vt C5 (pink) and Vt C5-GFP – Vt C5 (green) are displayed as isosurfaces contoured at  $15\sigma$ . The fusion sites for GFP constructs are labeled and displayed in space-filling representation in the same color as the corresponding difference maps. Density tentatively attributed to Vt rearrangements is magenta. (c) Colored as in b, a view highlighting the density on the actin surface. Actin 1 is displayed as an electrostatic potential surface map, contoured at  $\pm 10 K_b T/e$  (blue, positive; red, negative). (d) Colored as in b, a view of the Vt H4-H5 helical hairpin, which fits the density poorly. Asterisk highlights a clash with the actin surface.

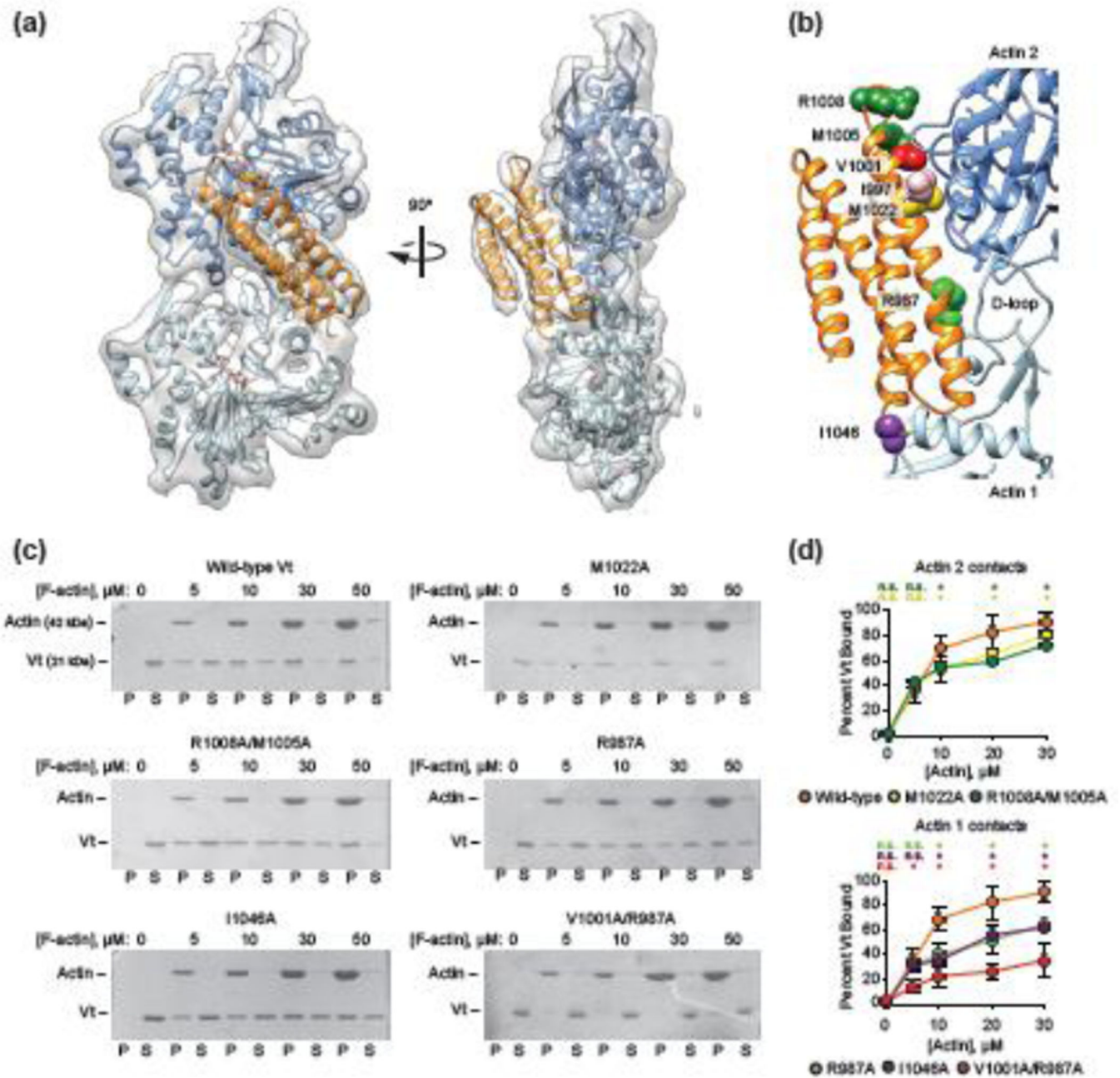


**Figure 3. MDFF model of the Vt-actin interface**

(a) The MDFF model (actin 1, light blue, actin 2, dark blue, Vt orange, ADP, pink) is shown in the segmented density map (transparent grey). (b) Colored as in a, residues that affect actin binding affinity are highlighted in space-filling representation and varying colors. (c) Representative SDS-PAGE analysis of high-speed co-sedimentation assays of Vt point mutants demonstrate impaired actin binding. Vt constructs, 10  $\mu$ M. P, pellet, S, supernatant. (d) Quantification of c. Error bars represent S.D.,  $n = 4$ . Asterisks indicated  $p < 0.01$  relative to wild-type control, t-test. N.s., not significant. Wild-type control is displayed on both plots for comparison purposes. (d) Representative SDS-PAGE analysis of low-speed actin

sedimentation assays demonstrate impaired actin bundling in the presence of Vt point mutants commensurate with impaired binding. Vt constructs, 10  $\mu$ M, actin, 20  $\mu$ M. P, pellet, S, supernatant. (e) Quantification of d. Error bars represent S.D., n = 4. Single asterisk indicates  $p < 0.05$ , double asterisk  $p < 0.01$  relative to wild-type control, t-test. All co-sedimentation assays were performed with full-length Vt constructs.

Author Manuscript

Author Manuscript

Author Manuscript

Author Manuscript

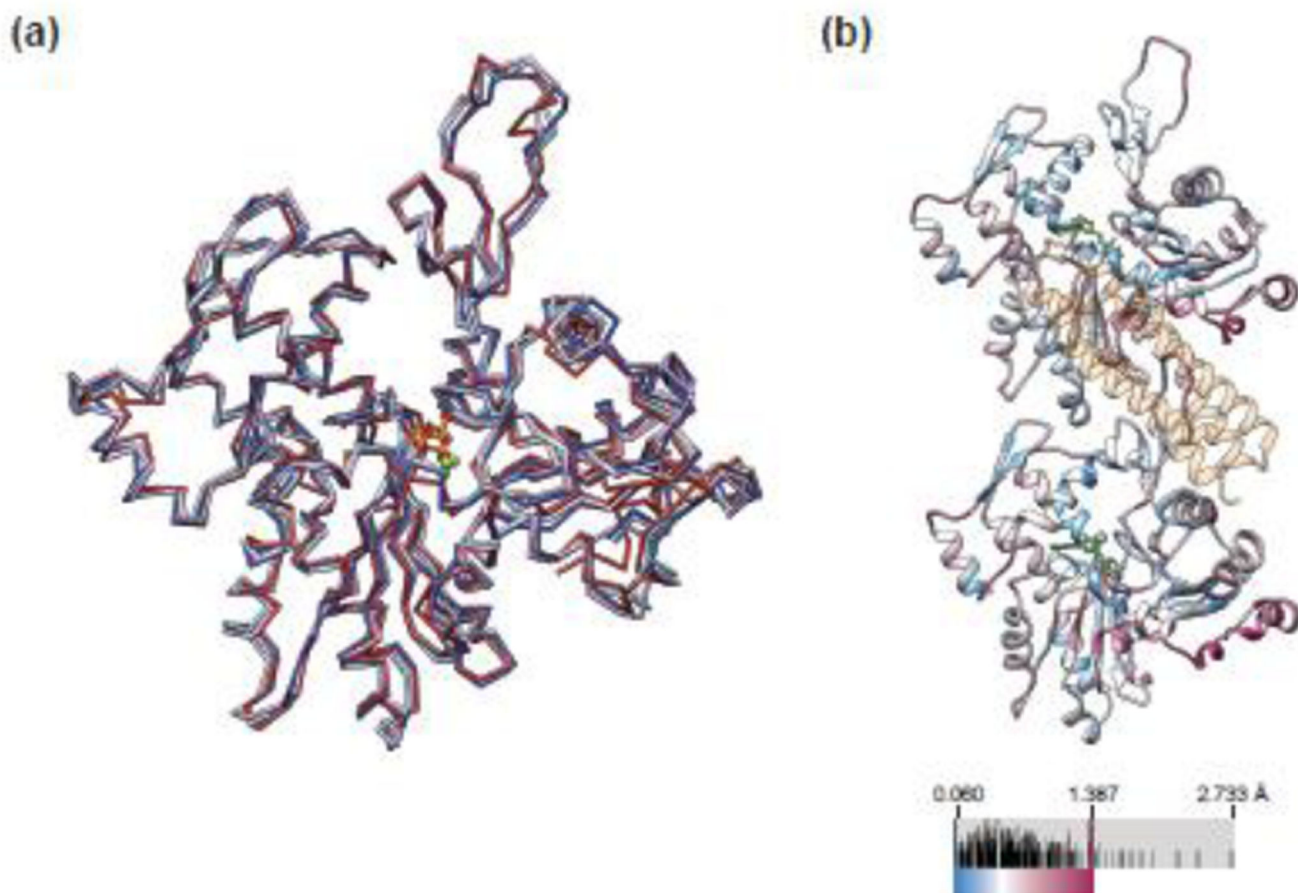


**Figure 4. Vt binding does not substantially alter the conformation of actin**

(a) Superposition of actin protomers from the Vt-actin MDFF model (light blue) with the actin alone MDFF model (light purple, 0.720 Å RMSD), the high-resolution structure of the actin-tropomyosin filament (PDB ID 3j8a, dark blue, 1.029 Å RMSD), and the high-resolution structure of F-actin (PDB ID 3j8i, dark red, 1.144 Å RMSD) (b) Actin from the Vt-actin MDFF model colored by per-residue C $\alpha$  RMSD when superimposed on the actin alone MDFF model (light blue vs. light purple in a). Vt is shown in transparent orange, ADP in green. Subtle differences are distributed throughout, with no obvious conformational changes occurring at the Vt binding site.



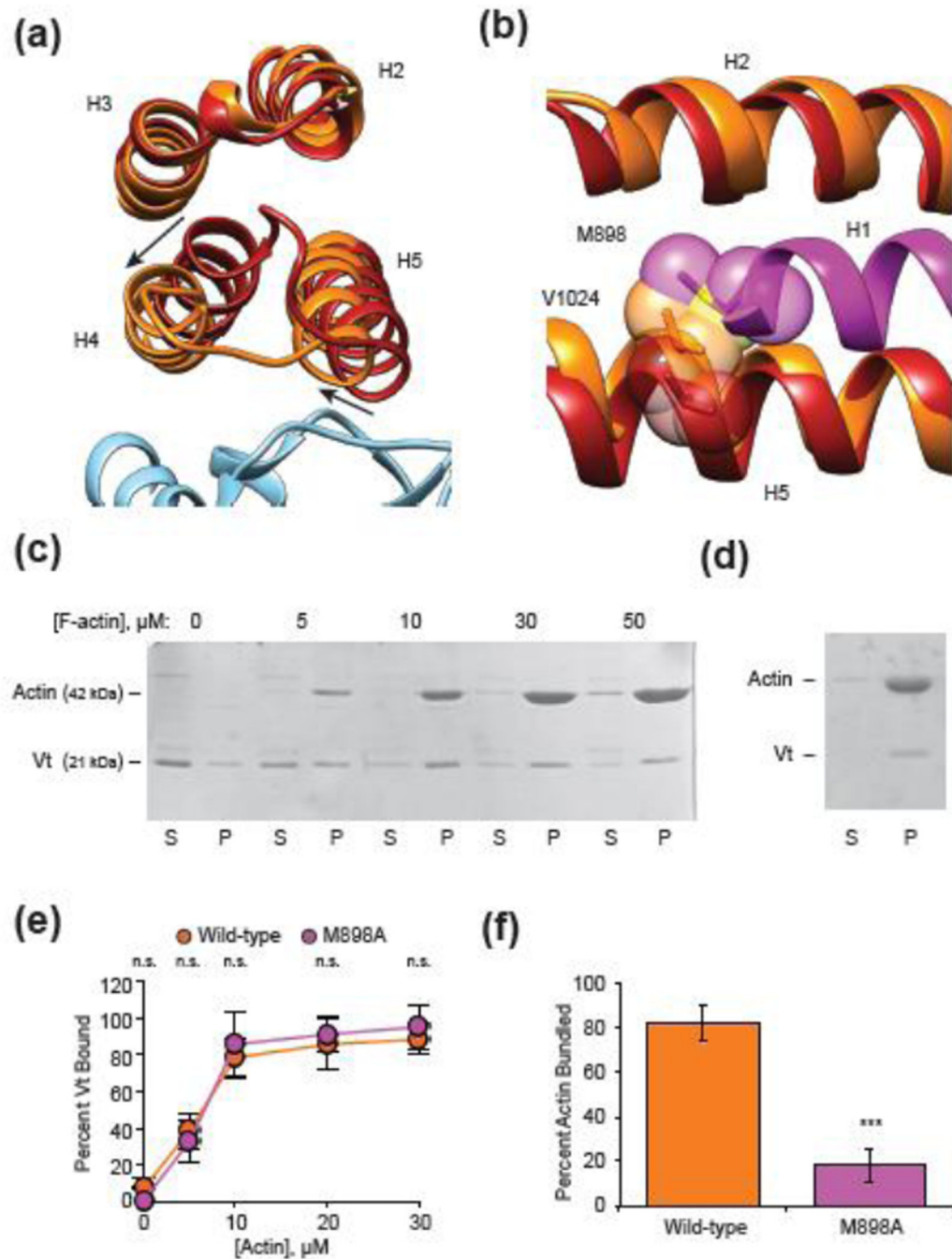


**Figure 5. A steric mechanism promotes H1 release to bundle actin**

(a) Superposition of the MDFF Vt model (orange; view from pointed end) with helices 2–5 of the rigid-body docked crystal structure of Vt (PDB 1QKR, red), highlighting the rearrangement of helices H4 and H5 to relieve clashes with actin (blue). (b) A view which highlights the clash of H1 (magenta) residue M898 with V1024 in the actin-bound state. (c) Representative SDS-PAGE of high-speed co-sedimentation assay demonstrates Vt M898A retains F-actin binding. Vt M898A, 10  $\mu$ M. S, supernatant, P, pellet. (d) Representative SDS-PAGE of low-speed co-sedimentation assay shows strongly impaired actin bundling of

Vt M898A. Vt M898A, 10  $\mu$ M, actin, 20  $\mu$ M. S, supernatant, P, pellet. (e) Quantification of c. Vt wild-type control redisplayed from Fig. 3d for comparison purposes. Error bars represent S.D., n = 3. N.s., not significant. (f) Quantification of d. Wild-type control redisplayed from Fig. 3e for comparison purposes. Actin, 20  $\mu$ M, Vt, 10  $\mu$ M. Error bars represent S.D., n = 10. Triple asterisk,  $p < 0.0001$  relative to wild-type control, t-test. All co-sedimentation assays were performed with full-length Vt constructs.

Author Manuscript

Author Manuscript

Author Manuscript

Author Manuscript



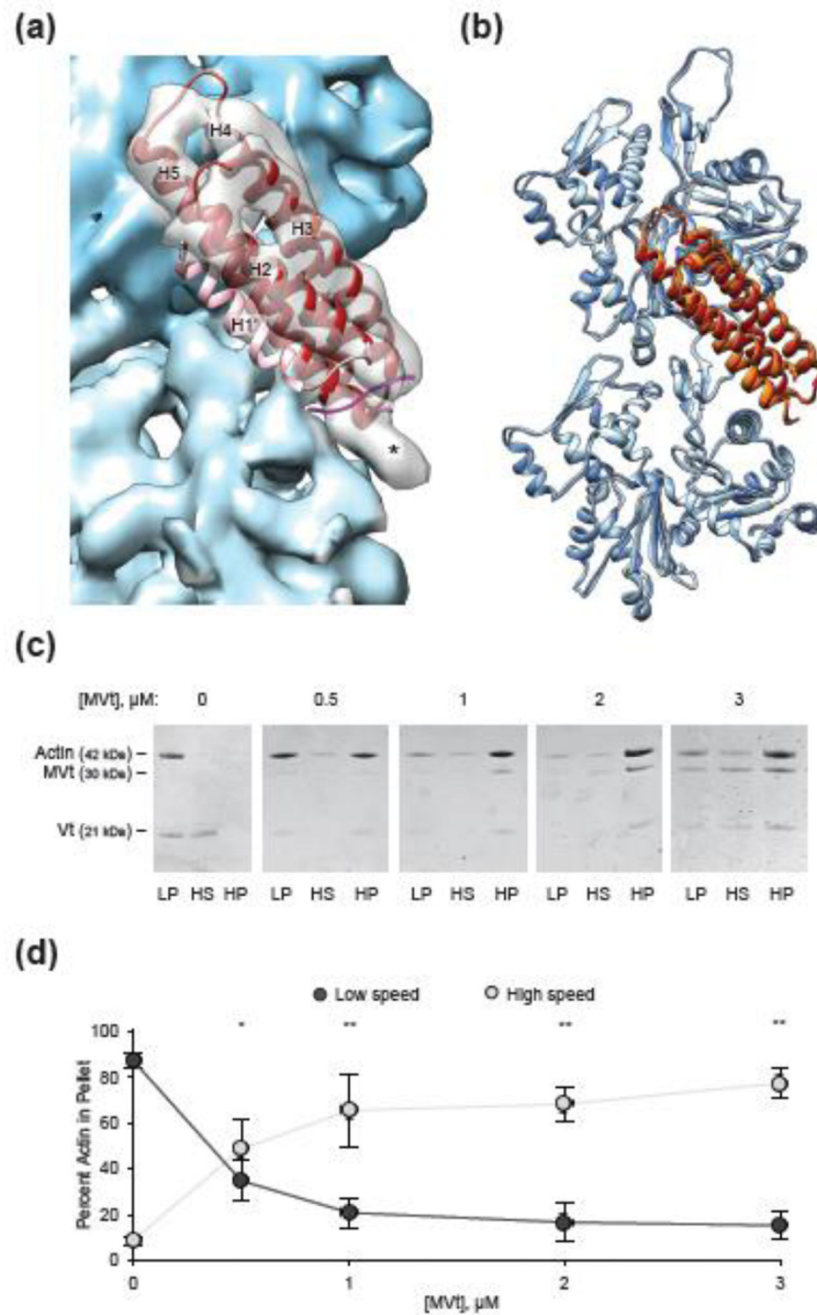


**Figure 6. MVt H1' is also released upon actin engagement to suppress actin bundling by Vt**  
 (a) Rigid-body docking of the MVt tail (firebrick) into the MVt C5-F-actin reconstruction (actin, blue, MVt, transparent grey). H1' is pink. Asterisk indicates unoccupied density. (b) Superposition of the MDFF models of MVt-actin and Vt-actin complexes, aligned on actin 1. Vt, orange, MVt, firebrick, actin from MVt-actin model, dark blue, actin from Vt-actin model, light blue. (c) Representative SDS-PAGE analysis of differential centrifugation assays of 3.0 μM actin in the presence of 3.0 μM Vt and the indicated amounts of MVt. (d) Quantification of c. Control condition of Vt alone is replotted from Supplementary Fig. 4h.

Error bars represent S.D., n = 3. Single asterisk,  $p < 0.05$ , double asterisk,  $p < 0.01$ , t-test vs. Vt alone. All co-sedimentation assays were performed with full-length MVt and Vt constructs.

Author Manuscript

Author Manuscript

Author Manuscript

Author Manuscript

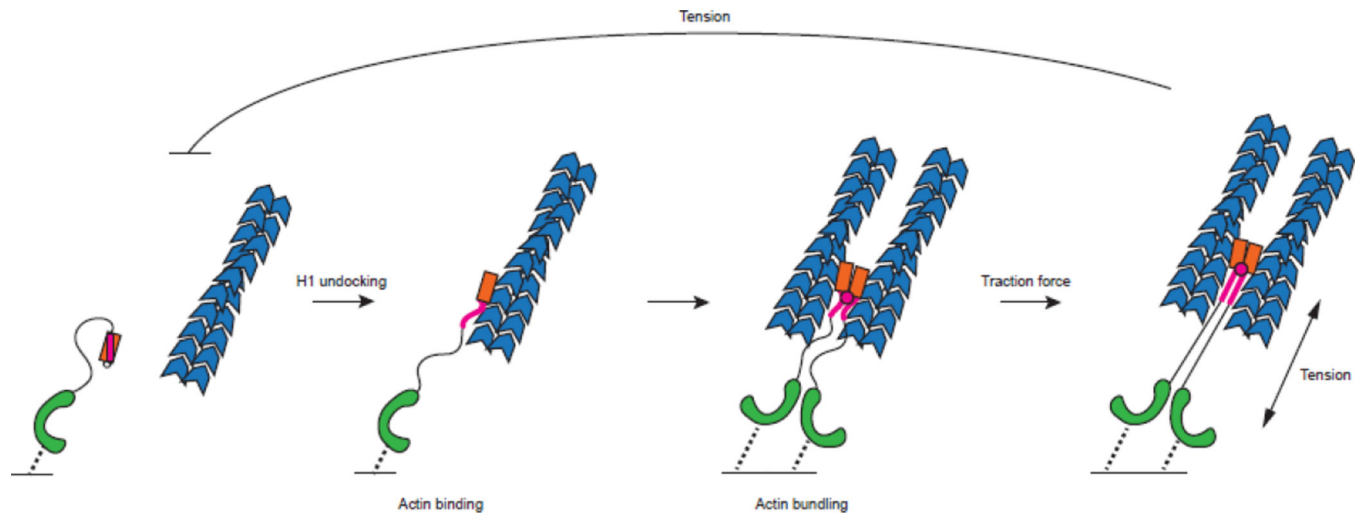


**Figure 7. Model of vinculin activation and tension reinforcing actin engagement**

Upon entering an adhesion, the interaction between Vh (green) and Vt (orange) is broken by engaging multiple binding partners (not shown). The linkage between Vh and the plasma membrane (black line) occurs through multiple layers of binding partners (i.e. talin, integrin, schematized as a dashed line, not to scale). H1 (magenta) must undock from the Vt bundle for Vt to engage actin. After actin binding and H1 release, Vt is capable of bundling actin (note: the detailed structure of the actin-induced Vt dimer structure remains unknown, magenta circle indicates an interaction). In this configuration, tension across the vinculin molecule will prevent H1 from re-docking, reinforcing actin binding and bundling.